



Facile spray-drying/pyrolysis synthesis of core–shell structure graphite/silicon-porous carbon composite as a superior anode for Li-ion batteries

Min Li ^{a,b,*}, Xianhua Hou ^{a,b,*}, Yujing Sha ^c, Jie Wang ^{a,b}, Shejun Hu ^{a,b}, Xiang Liu ^d, Zongping Shao ^e

^a School of Physics and Telecommunication Engineering, South China Normal University, Guangzhou 510006, China

^b Engineering Research Center of Materials and Technology for Electrochemical Energy Storage, Guangzhou 510006, China

^c State Key Laboratory of Materials-Oriented Chemical Engineering, Nanjing University of Technology, Nanjing 210009, China

^d Institute of Advanced Materials, Nanjing University of Technology, Nanjing 210009, China

^e Department of Chemical Engineering, Curtin University, Perth, WA 6158, Australia



HIGHLIGHTS

- A core–shell structure graphite/silicon-porous carbon composite was synthesized.
- The Si/C composite exhibited a capacity of 600 mAh g⁻¹ even after 100 cycles.
- The structure benefited electronic transfer and accommodated volume expansion.

ARTICLE INFO

Article history:

Received 22 July 2013

Received in revised form

15 September 2013

Accepted 5 October 2013

Available online 14 October 2013

Keywords:

Lithium-ion battery

Anode material

Silicon/graphite/amorphous carbon

composite

Spray drying

ABSTRACT

A silicon/graphite/amorphous carbon (Si/C) composite with a low silicon content in a core–shell structure has been easily synthesized using a simple method based on spray drying in combination with a subsequent pyrolysis process; natural graphite serves as the core, and silicon nanoparticles, which filled in the porous carbon matrix formed from the pyrolysis of citric acid and pitch precursors, serve as the shell. The combination of the core–shell structure for the composite and porous carbon-coating layer accommodates the large volume change of the silicon during the lithium intercalation/extraction process, thus stabilizing the electrode structure during discharge/charge cycles. As an anode material, the as-obtained Si/C composite demonstrates high capacity and excellent cycle stability. An initial specific discharge capacity of approximately 723.8 mAh g⁻¹ and a reversible specific capacity of approximately 600 mAh g⁻¹ after 100 cycles at a constant density of 100 mA g⁻¹ are reached, about two times the values for graphite. Due to the simple synthesis process and the excellent performance of the resulted electrode, great commercial potential is envisioned.

© 2013 Elsevier B.V. All rights reserved.

1. Introduction

Because of their several outstanding features, such as high energy density, high voltage, no memory effect, long cycling lifetime, and environmental benignity [1–3], rechargeable lithium-ion batteries (LIBs) have found increasing numbers of applications. They have become one of the most developed power sources for portable

application since the end of the 20th century. During recent decades, the potential applications of LIBs for large-scale electrochemical energy storage and as power batteries for electric vehicles (EVs) and hybrid electric vehicles (HEVs) have become very important. To date, carbon and graphite are the most commonly used anode materials for commercial LIBs due to their low price, their high conductivity, and high stability [4,5]. However, graphite provides a relatively low theoretical capacity of 372 mAh g⁻¹ [6,7], which limits its further application in higher-power systems such as EVs and HEVs. Therefore, new anode materials with high capacities and long lifespans have been intensively pursued and studied worldwide.

* Corresponding author. School of Physics and Telecommunication Engineering, South China Normal University, Guangzhou 510006, China. Tel.: +86 2039318011.

E-mail addresses: houxh@scnu.edu.cn (X. Hou), [\(Z. Shao\).](mailto:zongping.shao@curtin.edu.au)

A number of alternative anode materials, such as silicon [8–10], tin [11–13], and aluminum [14–16], have appeared in the recent open and patent literature. In particular, silicon-based anode materials are believed to be promising alternatives to commercial carbon/graphite in LIBs due to the high theoretical specific capacity of 4200 mAh g⁻¹ and low stable plateau potential (~ 0.4 V) for pure silicon [17,18]. Unfortunately, silicon in the bulk phase as an anode suffers badly from poor cycling performance [19,20], due to the large volume variation of the electrode, which can reach as high as 400%, during the charge/discharge process. Such a large volumetric variation could cause the pulverization of the electrode material, inducing quick capacity decay. Until now, considerable efforts have been made to improve the electrochemical performance of silicon-based anodes. Nano-crystallization and carbon coating of silicon have been proposed as effective methods [21–25]. However, nano-sized silicon particles aggregate easily because of their high surface energy. Hence, the dispersal of nano-sized silicon becomes a key challenge for the practical use of silicon anodes in LIBs.

The overall capacity of a battery is determined by both its anode and its cathode but mainly by the electrode with the lower capacity. Therefore, the anode capacity may not need to be as high as the theoretical capacity of silicon if the cathode capacity is relatively low. For example, by applying LiFePO₄ as a cathode material with a theoretical capacity of approximately 170 mAh g⁻¹, we may use a composite of graphite and silicon to provide affordable anode capacity with minimized anode volume expansion. For example, for a composite of 20% silicon and 80% graphite, the theoretical capacity can still reach ~ 1137.6 mAh g⁻¹, which is much higher than the capacity of LiFePO₄, while the overall volume expansion of the anode is reduced to only 160% rather than the 400% of a pure silicon electrode, suggesting that improved cycling stability could be reached by using a silicon composite electrode instead of pure silicon. Indeed, previous studies have proved that the composite of nano-silicon and graphite could partly alleviate the mechanical stresses induced by the severe volumetric changes of silicon [26–28], which correlate strongly with the electrochemical performance of the anode material. However, the graphite is not the very perfect one acting as the matrix to buffer the volume expansion of silicon. Previously, we proposed the formation of an amorphous carbon–silicon composite electrode by the pyrolysis of a citric acid–silicon slurry, prepared from high energy ball milling. Using this method, improved capacity and good cycling performance were achieved [29]. However, the carbon formed from the pyrolysis of citric acid is usually not well crystallized and shows relatively low conductivity and poor mechanical strength.

In this study, a core–shell structure graphite/Si-porous carbon composite was prepared easily by the spray drying/pyrolysis of a slurry composed of nano silicon, graphite, and citric acid (pitch). Both graphite and silicon served as the main electro-active components of the anode, while porous carbon, produced from the pyrolysis of citric acid/pitch, performed several functions, including acting as the matrix to accommodate the silicon, providing buffer space for the silicon, acting as a barrier to suppress the aggregation of nano-sized silicon, and providing free channels for liquid electrolyte penetration to maximize the electro-active areas of the graphite and silicon. The graphite also played the additional role of providing sufficient electrical conductivity and mechanical strength. As a result, high electrical conductivity, high stability during solid–electrolyte interface formation, and good structural integrity were all achieved for the novel graphite/Si-porous carbon composite, which demonstrated an initial discharge capacity of 723.8 mAh g⁻¹ (about two times the theoretical capacity of graphite), $\sim 94.9\%$ capacity retention over 100 cycles, and good rate performance.

2. Experimental

2.1. Synthesis of novel core–shell porous Si/C composite

The weight ratio of natural graphite to silicon to amorphous carbon source in the raw materials for the synthesis of the novel core–shell structure sample was designed as 72:10:18. Both citric acid and pitch served as the organic precursors, with the ratio of 10:3, to the pyrolyzed carbon. The preparation procedure for the novel graphite/Si-porous carbon composite is illustrated in Scheme 1. First, nano-silicon particles and polyvinylpyrrolidone (PVP) were mixed in ethanol under ultrasonic vibration for 1 h to form a homogeneous suspension. Then, the suspension and the appropriate proportion of natural graphite were dropped into a citric acid–ethanol solution. After continuous magnetic stirring for 1 h, the resulting colloid was spray dried to form a solid precursor under the following conditions: the rotation speed of the centrifugal atomizer was 35,000 rpm; the rate of suspension delivery was 15 mL min⁻¹; the inlet temperature of the spray dryer was 120 °C; and the outlet temperature was 80 °C. The as-prepared Si/organic precursors were then pre-decomposed at 380 °C for 4 h in a quartz tube furnace under an N₂ atmosphere. Then, the primary powder products were further mixed with a pitch tetrahydrofuran (THF) solution to form a slurry, which was further spray dried using the same procedure as before. The ratio of citric acid to pitch organic precursors was fixed at 10:3. The obtained solid precursor was then fired at 500 °C for 3 h and then at 900 °C for another 3 h in a quartz tube furnace under an N₂ atmosphere to obtain a graphite/Si-porous carbon composite in powder form. The resulting composite was ground and sieved for the fabrication of the electrode.

2.2. Materials characterization and electrochemical test

The crystal structure, cross-sectional morphology, and microstructural morphology of the as-prepared Si/C composite were characterized by X-ray diffraction (XRD; PANalytical X'Pert PRO, Cu/K_α radiation, $\lambda = 1.5406$ nm), scanning electron microscopy (SEM; ZEISS ULTRA 55), ion milling system (Hitachi E-3500), and transmission electron microscopy (TEM; JEM-2100HR). The carbon content in the Si/C composite was determined by the oxygen-temperature-programmed oxidation (O₂-TPO) technique. Cyclic voltammetry measurements were carried out using a Solartron 1470E electrochemistry system at a scan rate of 0.1 mV s⁻¹. The charge–discharge performance of the cells was tested in a voltage range of 0.01–1.0 V vs. Li/Li⁺ at a constant current of 100 mA g⁻¹. The electrochemical performance was measured using CR2430 button cells. The working electrode was made by mixing 80 wt.% Si/C composite, 10 wt.% Super P as the conducting agent, and 10 wt.% LA132 as the binder. The electrode slurry was dispersed and spread onto copper foil (10 μm). After drying under vacuum at 80 °C for 12 h, the electrodes were pressed and punched ($\phi = 18$ mm). The average mass loading of the electrodes was approximately 2.16 mg. And the electrode density was calculated to 8.49×10^{-4} g cm⁻². CR2430 button cells were assembled in an argon-filled glove box using 1 M LiPF₆ in a mixture of EC/DEC/EMC (1:1:1 by volume) as the electrolyte, using Celgard-2400 as the separator, and metallic lithium foil as the counter and reference electrode.

3. Results and discussion

3.1. Phase composition

The X-ray diffraction (XRD) patterns of the as-prepared Si-based composite from the spray drying/pyrolysis process are shown in Fig. 1a. For comparison, the XRD patterns of graphite and silicon are



Scheme 1. The preparation procedure for the novel graphite/Si-porous carbon composite.

also presented. Two hexagonal phases with space groups of P_{6_3}/mmc (C_{G1}) and $R-3m$ (C_{G2}) can be found in the raw graphite material, while the silicon phase was indexed with a single cubic phase ($Fd-3m$). The diffraction peaks of the Si-based composite can be well indexed based on a physical mixture of graphite and silicon crystalline phases. Due to the lamellar structure of graphite, the intensity of the peak belonging to the graphite phases at

approximately 26.5° was much stronger than the rest peaks. The peaks at 2θ of 28.4° , 47.3° , 56.1° can be assigned to the diffraction planes of (111), (220), (311) for elemental silicon, respectively. The weak intensity of the silicon diffraction peaks can be explained by the relatively low content of silicon (~10 wt.% as targeted) in the composite. No peak corresponding to SiO_2 (oxidation product of silicon) or SiC (product from the reaction between Si and C) was detected from the XRD pattern, which suggests that the oxidation of silicon and the chemical reaction between silicon and carbon during the preparation were minimized by conducting the pyrolysis under inert gas atmosphere at $900^\circ C$, low enough to avoid the reaction between Si and C/O. In addition to the above important and obvious diffraction peaks, a broad peak that covered a large 2θ range from 15 to 35° , centered at approximately 23° , and overlapped the (002)/(111) diffraction peaks of graphite at 26.4° and the (111) diffraction peak of silicon at 28.4° was also observed. It is the characteristic diffraction peak of amorphous carbon, which likely resulted from the pyrolysis of citric acid and pitch [30].

Rietveld refinement of the XRD patterns was then conducted based on a mixture phase of Si and graphite, and the results are shown in Fig. 1b. During the refinement, the above mentioned three phases (two graphite phases and one silicon phase) were included. The reliability factors of $R_{wp} = 8.14\%$ and $R_p = 5.83\%$ with goodness of fit $\chi^2 = 24.14$ were obtained. The quantitative analysis revealed that the contents of the three phases were 55.6% for C_{G1} ($a = b = 2.4622(8)$, $c = 6.712(5)$, $\alpha = \beta = 90^\circ$, $\gamma = 120^\circ$), 31.2% for C_{G2} ($a = b = c = 3.64(3)$, $\alpha = \beta = \gamma = 39.36(7)^\circ$), and 13.2% for the silicon phase ($a = b = c = 5.43(0)$, $\alpha = \beta = \gamma = 90^\circ$). The refined mass ratio of the silicon and graphite in the Si/C composite is 13.2:86.8, which was close to the set value of 10:90.

To further support the simultaneous presence of silicon, graphite, and amorphous carbon in the composite, the sample was studied using Raman spectroscopy. For comparison, the Raman spectra of pure silicon and of graphite are also presented. As shown in Fig. 2, pure silicon demonstrated a main sharp adsorption band at a Raman shift of 515 cm^{-1} and two small adsorption bands at 295 and 950 cm^{-1} , while the graphite showed two characteristic bands at 1351 and 1601 cm^{-1} , the D band and G band, respectively. The D band usually results from carbon with lattice defects, disordered carbon at the edge and low-symmetry carbon, which can be assigned to the A_{1g} vibration mode of nanocrystalline graphite, while the G band results from the stretch vibration of sp^2 hybrid carbon in carboatomic rings or long chain carbon, which belongs to the E_{2g} vibration mode. The ratio of the integrated area of the D band and the G band, R (I_D/I_G), reflects the graphitization degree. A lower R value means a higher graphitization degree of the carbon. The R value of graphite is only 0.35, suggesting a high degree of graphitization, as expected. For the as-prepared Si and the graphite and amorphous carbon composite from the spray drying/pyrolysis process, three Raman shift bands were observed. There was one sharp peak at 515 cm^{-1} , which was assigned to elemental silicon. A broad band at 1351 cm^{-1} and a sharp band at 1601 cm^{-1} also

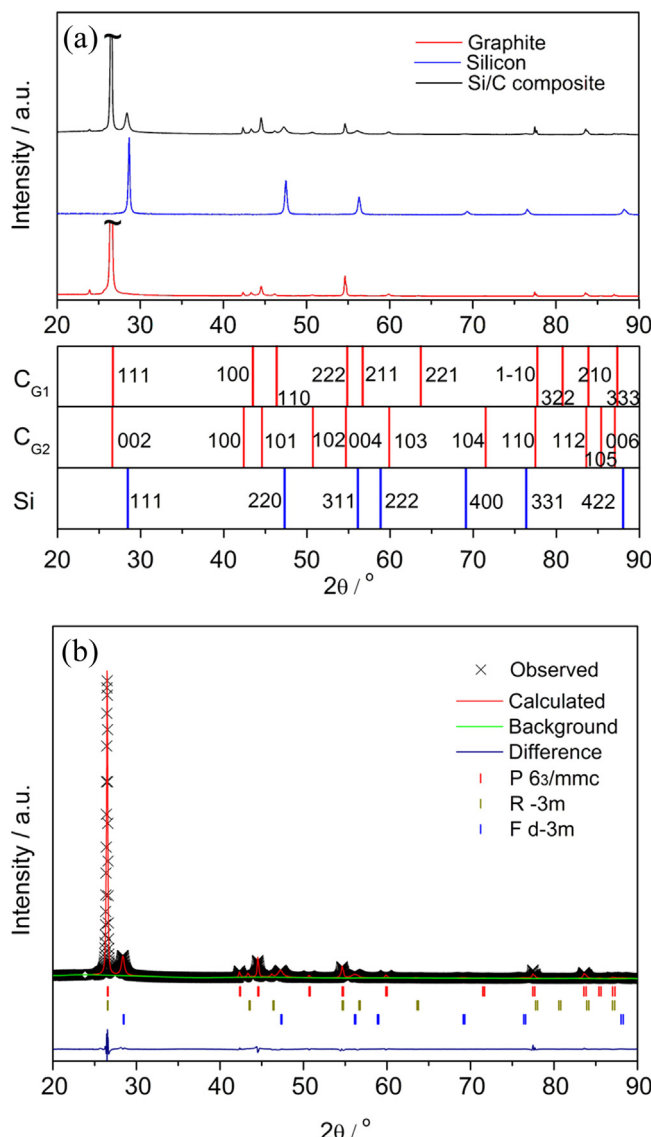


Fig. 1. (a) The XRD diffraction patterns of silicon, graphite, and Si/C composite, respectively. (b) The Rietveld refinement for Si/C composite.

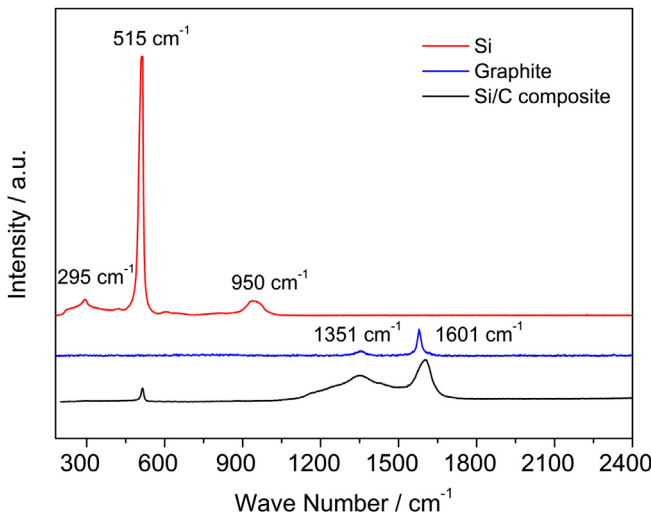


Fig. 2. The Raman spectrum of pure silicon, natural graphite, and Si/C composite.

appeared and are attributed to the carbon phase in the composite. In contrast to graphite, the intensity of the D band in the composite was much enhanced and the calculated R value increased to 1.50, compared to 0.35 for graphite, suggesting increased disorder of the carbon in the composite compared to graphite, which is obviously the contribution of the carbon pyrolyzed from citric acid and pitch.

The total amount of carbon in the composite was analyzed by the oxygen-temperature-programmed oxidation (O₂-TPO) technique [29,31,32]. Fig. 3 shows the typical O₂-TPO profile in the CO₂ signal of the sample. A higher temperature for carbon oxidation means a higher graphitization degree of the carbon. Two CO₂ peaks appeared in the O₂-TPO profile, one at approximately 510 °C and the other at approximately 802 °C. These two peaks suggest there are two types of carbon in the samples, agreeing well with the observations from the XRD and Raman spectra. The amount of carbon in the composite, determined from the CO₂ peak area, was approximately 92 wt.%, suggesting that the real composition of the composite is 92 wt.% (graphite + amorphous carbon) and 8 wt.% silicon, which is similar to the targeted values. In combination with the XRD results, the ratio of graphite to silicon to amorphous carbon should be 53:8:39.

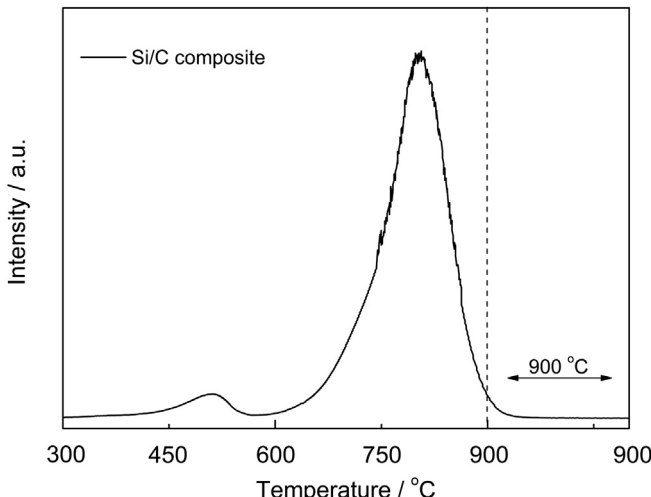


Fig. 3. Typical O₂-TPO profile of the as-prepared Si/C composite.

3.2. Particulate morphology

The microscopic morphology of the samples was observed by SEM and TEM. Fig. 4a shows a typical SEM image of the elemental silicon raw material. The particles were 200 nm in diameter and were somewhat aggregated due to the high surface energy of the nanoparticles. According to the TEM image, in the insert of Fig. 4a, the primary Si particles had a particle size of 30–50 nm, which formed secondary particles with a size of approximately 200 nm, as observed in the SEM image. The natural graphite had an irregular shape with relatively sharp boundaries and demonstrated a layered structure (Fig. 4b) with a relatively smooth, dense surface. The size of the graphite was relatively large, up to approximately 10 μm. For the composite prepared from the spray drying/pyrolysis process, as shown in Fig. 4c, the main particles showed a similar particulate shape to the graphite and a similar size of approximately 10 μm; however, the particle surface was much rougher, and the particle boundaries were more round. In addition to the large particles, some small particles with perfect spherical shapes and a much smaller size of 1–3 μm were also observed. An image at greater magnification of a large particle is shown in Fig. 4d and clearly shows that the particle surface had a highly porous structure. A similar surface morphology was also observed for the smaller round particles. Some individual large-sized particles were then cut to determine the micro-structural characteristics of their interior. Fig. 4e shows a typical SEM image of a cross-section of the particles, demonstrating that the particle was composed of a dense core and a porous shell. The core clearly showed a somewhat layered structure, which is typical of graphite, suggesting the graphitic nature of the core. Over the core surface, a shell with a thickness of 1–3 μm was observed, and the shell had a porous morphologic structure. Clearly, the porous shell was primarily formed from the thermal decomposition of citric acid and pitch.

To further support the formation of the shell structure, we peeled the shell layer off the particle, using a surface mechanical milling treatment, for TEM observation, as shown in Fig. 5a–d. It could be seen from Fig. 5a–d that the composite particles comprised three phases of graphite, silicon, and carbon. The TEM, shown in Fig. 5a and b, demonstrated that some darker particles with a size of approximately 200 nm were embedded in the shell layer, in connection with the results as shown in Fig. 4a, and were likely to be the silicon particles. These particles were coated homogeneously by amorphous carbon decomposed from citric acid and pitch, which provided a buffer to accommodate the volume change during the charge–discharge process of silicon and to increase current collection for the nano-sized silicon, thus improving the cycling performance; In the HR-TEM image (Fig. 5c and d), distinct diffraction fringes with spacings of 0.342 nm and 0.313 nm were observed, corresponding to the (002) diffraction plane of the graphite and the (111) diffraction plane of the silicon. In the corresponding SAED pattern, as shown in the inset of Fig. 5d, the diffraction rings assignable to the diffraction planes Si (111), Si (331), and graphite (101) were observed, further suggesting the specific composition of the shell.

To obtain further information about the porous structure of the composite, it was subjected to BET surface area measurement; for comparison, the results of natural graphite are also presented. Fig. 6a shows the nitrogen adsorption–desorption isotherm of the natural graphite. It shows a type-III isotherm according to the International Union of Pure and Applied Chemistry classification, suggesting the nonporous nature of the material. The insert in Fig. 6a shows the pore size distribution curve of the graphite. The material demonstrated almost no pores, with a calculated pore volume of only 1.1 cm³ g⁻¹. As a result, a specific surface area of only 4.8 m² g⁻¹ was obtained. For the core–shell structure Si–graphite–porous carbon composite, as shown in Fig. 6b, the nitrogen

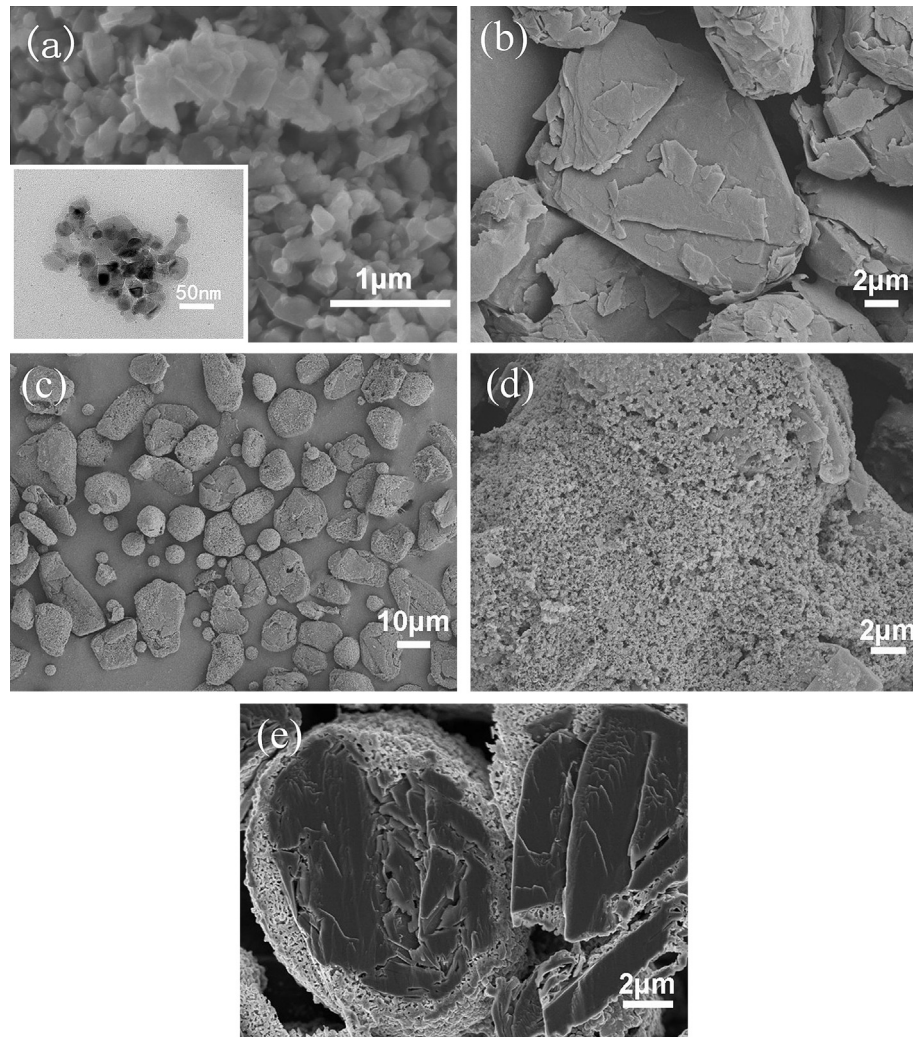


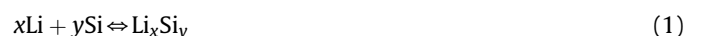
Fig. 4. (a) Typical SEM and TEM (the inset one) profiles of silicon raw materials for preparation of Si/C composite; (b) typical SEM image of natural graphite; (c)–(e): SEM image, magnified surface image, and cross profile of the novel core–shell porous Si/C composite, respectively.

adsorption–desorption isotherm shows a type-IV isotherm, which was much different from the results for graphite. Between P/Po of 0.4–1.0, a distinct hysteresis loop was observed, suggesting the presence of mesopores and macropores. According to the pore size distribution curve, shown in Fig. 6b insert, mesopores with a narrow size distribution from 3 to 6 nm peaking at 4 nm were identified. Based on the SEM and TEM images, such these pores were likely from the porous shell layer. The specific surface area of the sample reached $12.2 \text{ m}^2 \text{ g}^{-1}$, which was almost three times the specific surface area of the natural graphite. Clearly, the increased surface area was a result of the nano-sized silicon and the porous carbon pyrolyzed from the citric acid and pitch organic precursor.

3.3. Electrochemical performance

The as-prepared core–shell structure graphite/Si-porous carbon material was used to produce an anode for an electrochemical performance test in a two-electrode cell configuration. Fig. 7 presents the typical cyclic voltammogram curves of the composite anode and the natural graphite (the inset one), measured in the voltage range of 0–1.5 V (vs. Li/Li⁺) at a scanning rate of 0.1 mV s⁻¹. In the first cycle, a broad cathodic peak ranging from 0.3 to 0.9 V

was observed, indicating the formation of SEI over the surface of the electrode from the decomposition of the liquid organic electrolyte, but this peak was absent in subsequent cycles. In the second and subsequent cycles, the shape of the cyclic voltammogram curve changed to a lesser extent, suggesting that the reversibility of insertion and extraction in the core–shell structure composite was much improved. The sharp cathodic peak below 0.2 V and the anodic peaks between 0.1 and 0.6 V were related to the insertion and extraction reactions of Li⁺ with natural graphite and silicon, respectively. For the reduction process, the peaks of natural graphite and silicon overlapped in the range of 0.1–0.3 V, corresponding to the formation of Li_xC_6 and Li_xSi_y , as indicated in Eqs. (1) and (2) [33], respectively. For the oxidation process, the reaction of natural graphite is different from the reaction of silicon. As can be seen from the CV of the natural graphite (the inset of Fig. 7), an expected oxidation peak at approximately 0.2 V was observed, whereas only one small peak at 0.5 V was shown for silicon, which resembled the graphite–silicon composite reported in the literature [34].



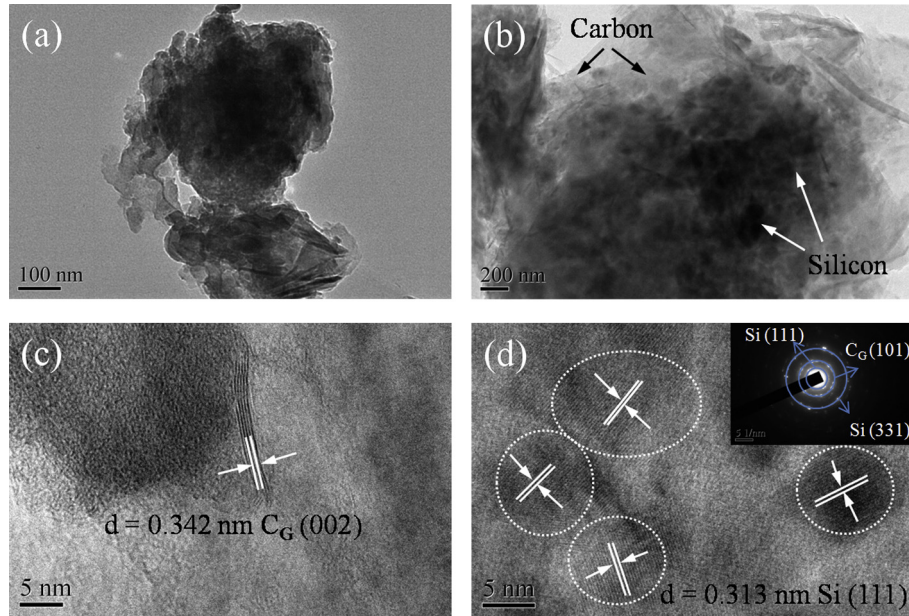


Fig. 5. TEM images of the peeled shell part of Si/C composite (a) in full size, (b) in partial enlarged view, (c)–(d) the HRTEM images of the shell part. The inset of (d) shows the corresponding SAED image of the as-prepared Si/C composite.

Fig. 8 illustrates the discharge–charge curves of the composite electrode, including the 1st cycle, 2nd cycle, 45th cycle, and 100th cycle. The discharge and charge capacity of the composite electrode were 723.8 mAh g^{-1} and 538.1 mAh g^{-1} , respectively, in the first cycle, indicating an irreversible capacity loss of only 25%. To a certain extent, the irreversible capacity of the first cycle can be attributed to the formation of a solid electrolyte interface (SEI) layer on the surface of the electrode at 0.6–0.9 V. In this experiment, the high capacity of the composite electrode was due to the presence of nano-sized silicon. The discharge capacity value of the 100th cycle remained as high as 592.4 mAh g^{-1} . Compared with the average value of the initial three cycles, the capacity retention rate was 94.9% even after 100 cycles. **Fig. 8** also shows that a stable discharge plateau at 0.15 V evolved from the second cycle, which remained stable in the subsequent processes. Furthermore, aside from the first cycle, the discharge capacity of the composite electrode in each cycle was only slightly higher than the charge capacity in the previous cycle, which is quite different from the rapid capacity decay of a conventional pure silicon electrode [35].

Fig. 9 shows the specific capacity and columbic efficiency vs. the cycle numbers of the composite and the cycling performance of

natural graphite. Compared to natural graphite, the as-fabricated core–shell structure graphite/Si-porous carbon composite as an anode demonstrated a higher specific capacity and maintained an excellent cycling stability. Specifically, the capacity increased gradually and reached a maximum discharge capacity of 651.3 mAh g^{-1} at the 45th cycle, which was likely associated with a surface activation process. Subsequently, the discharge–charge capacity decreased slowly, but the discharge capacity remained as high as 592.4 mAh g^{-1} after 100 cycles, and the columbic efficiency remained over 99.5%.

The excellent electrochemical performance of the composite electrode can be explained based on the following considerations. First, cheap natural graphite was used as a mechanical support and also acted as an active electrode component for providing the lithium insertion host, thus increasing the electrical conductivity; second, the introduction of nano-sized silicon increased the overall capacity due to the ultrahigh theoretical capacity of silicon (4200 mAh g^{-1}); third, the use of porous carbon as a matrix provided a buffer to accommodate the volume change during the charge–discharge process of silicon and to increase current collection for the nano-sized silicon, thus improving the cycling

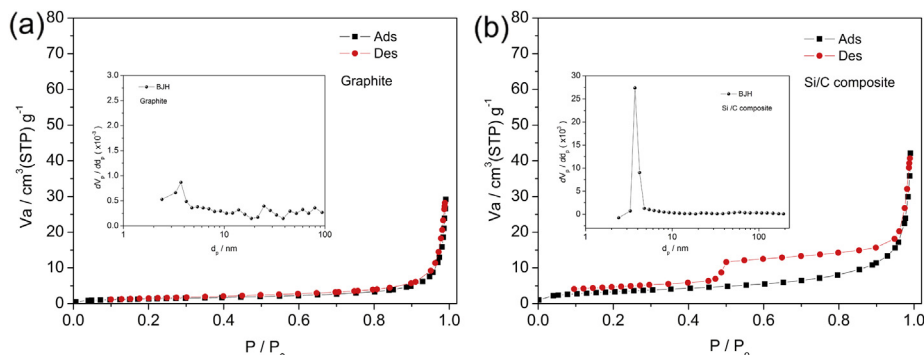


Fig. 6. N_2 adsorption–desorption isotherms of (a) graphite and (b) Si/C composite. The inset BJH images reflect the corresponding pore size distributions.

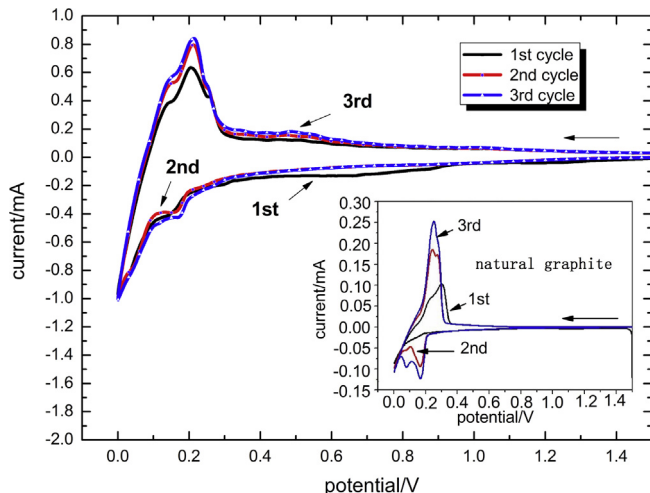


Fig. 7. Cyclic voltammogram of the novel core–shell porous Si/C composite electrode and the natural graphite (the inset one) measured in the voltage range of 0–1.5 V at a scan rate of 0.1 mV s^{-1} for the first, second, and third cycles.

performance; and fourth, the porous structure of the shell with mesopores allowed penetration of liquid electrolyte to the graphite core, ensuring a high electro-active area for the graphite.

4. Conclusions

In summary, a spray drying method was successfully utilized to fabricate a novel core–shell composite with a graphite core and nano-sized silicon embedded in a porous carbon shell that was a superior anode in lithium-ion batteries. The novel core–shell structure composite accommodated the large volume change of the electrode during discharge/charge. In addition, the citric acid and pitch pyrolyzed carbon coated the surface of the natural graphite perfectly and constructed a connected network of graphite and nano-silicon particles. Moreover, the organic carbonization, which was interconnected with nano-silicon, also enabled a high electrical conductivity and improved the formation of the solid–electrolyte interface and the structural integrity.

Compared with pure silicon and graphite anodes, the novel core–shell porous Si/C composite had the best combination of

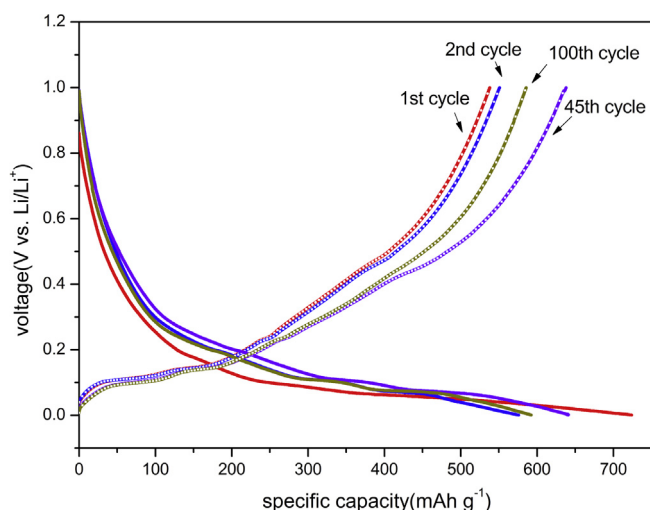


Fig. 8. Discharge–charge curves of the novel core–shell porous Si/C composite, including the 1st cycle, 2nd cycle, 45th cycle, and 100th cycle.

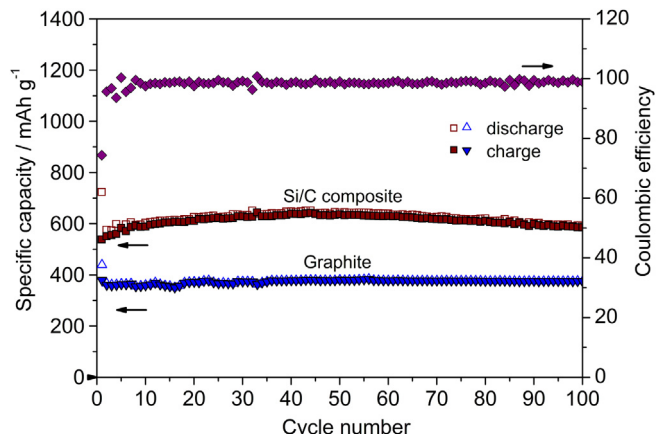


Fig. 9. The cycle performance and coulombic efficiency of natural graphite and the as-prepared Si/C composite at a constant current of 100 mA g^{-1} for 100 cycles.

reversible capacity, initial efficiency, and cycling stability, and this anode material exhibited excellent electrochemical performance. The Si/C composite had a fairly high reversible capacity of 723.8 mAh g^{-1} with an initial efficiency of 75.2%, a maximum discharge capacity of 651.3 mAh g^{-1} at the 45th cycle, and a surprisingly high discharge capacity at the 100th cycle at 592.4 mAh g^{-1} . Meanwhile, spray drying is an environmentally friendly, economical, and relatively high-yield method for the production of the Si/C composite in large quantities. Consequently, the novel core–shell structure composite electrode may be a potential alternative to graphite for high energy density lithium-ion batteries.

Acknowledgments

This work was financially supported by the National Science Foundation of China (NSFC, Nos. 51201066 and 51171065), Natural Science Foundation of Guangdong Province (Nos. S2012020010937, 10351063101000001), Foundation for Distinguished Young Talents in Higher Education of Guangdong (No. 2012LYM_0048). Dr Zongping Shao Acknowledges ARC future fellowship.

References

- [1] A.M. Skundin, O.N. Efimov, O.V. Yarmolenko, Russ. Chem. Rev. 71 (2002) 329–346.
- [2] V. Etacheri, R. Marom, R. Elazari, G. Salitra, D. Aurbach, Energy Environ. Sci. 4 (2011) 3243–3262.
- [3] G. Jeong, Y.U. Kim, H. Kim, Y.J. Kim, H.J. Sohn, Energy Environ. Sci. 4 (2011) 1986–2002.
- [4] J. Yang, X.Y. Zhou, J. Li, Y.L. Zou, J.J. Tang, Mater. Chem. Phys. 135 (2012) 445–450.
- [5] H. Nozaki, K. Nagaoka, K. Hoshi, N. Ohta, M. Inagaki, J. Power Sources 194 (2009) 486–493.
- [6] Q. Si, K. Hanai, T. Ichikawa, A. Hirano, N. Imanishi, Y. Takeda, O. Yamamoto, J. Power Sources 195 (2010) 1720–1725.
- [7] J.M. Tarascon, M. Armand, Nature 414 (2001) 359–367.
- [8] S.H. Ng, J. Wang, K. Konstantinov, D. Wexler, S.Y. Chew, Z.P. Guo, H.K. Liu, J. Power Sources 174 (2007) 823–827.
- [9] H.S. Kim, K.Y. Chung, B.W. Cho, J. Power Sources 189 (2009) 108–113.
- [10] Q. Si, K. Hanai, T. Ichikawa, A. Hirano, N. Imanishi, O. Yamamoto, Y. Takeda, J. Power Sources 196 (2011) 6982–6986.
- [11] J. Hassoun, D.J. Lee, Y.K. Sun, B. Scrosati, Solid State Ionics 202 (2011) 36–39.
- [12] J.Z. Chen, L. Yang, S.H. Fang, S. Hirano, Electrochim. Commun. 13 (2011) 848–851.
- [13] S. Brutt, J. Hassoun, B. Scrosati, C.Y. Lin, H. Wu, H.W. Hsieh, J. Power Sources 217 (2012) 72–76.
- [14] W.C. Zhou, S. Upadhyay, M.S. Whittingham, Electrochim. Commun. 13 (2011) 158–161.
- [15] M.J. Lindsay, G.X. Wang, H.K. Liu, J. Power Sources 119–121 (2003) 84–87.
- [16] X.F. Lei, C.W. Wang, Z.H. Yi, Y.G. Liang, J.T. Sun, J. Alloys Compd. 429 (2007) 311–315.
- [17] T. Zhang, J. Gao, H.P. Zhang, L.C. Yang, Y.P. Wu, H.Q. Wu, Electrochim. Commun. 9 (2007) 886–890.

- [18] H.C. Tao, L.Z. Fan, X.H. Qu, *Electrochim. Acta* 71 (2012) 194–200.
- [19] U. Kasavajjula, C.S. Wang, A.J. Appleby, *J. Power Sources* 163 (2007) 1003–1039.
- [20] J.C. Guo, A. Sun, X.L. Chen, C.S. Wang, A. Manivannan, *Electrochim. Acta* 56 (2011) 3981–3987.
- [21] K. Hanai, Y. Liu, N. Imanishi, A. Hirano, M. Matsumura, T. Ichikawa, Y. Takeda, *J. Power Sources* 146 (2005) 156–160.
- [22] Y.N. Jo, Y. Kim, J.S. Kim, J.H. Song, K.J. Kim, C.Y. Kwag, D.J. Lee, C.W. Park, Y.J. Kim, *J. Power Sources* 195 (2010) 6031–6036.
- [23] L.W. Zhao, S.H. Han, S. Okada, B.K. Na, K. Takeno, J. Yamaki, *J. Power Sources* 203 (2012) 78–83.
- [24] M.K. Datta, P.N. Kumta, *J. Power Sources* 165 (2007) 368–378.
- [25] B.C. Kim, H. Uono, T. Sato, T. Fuse, T. Ishihara, M. Senna, *Solid State Ionics* 172 (2004) 33–37.
- [26] W. Wang, P.N. Kumta, *J. Power Sources* 172 (2007) 650–658.
- [27] L.B. Chen, X.H. Xie, B.F. Wang, K. Wang, J.Y. Xie, *Mater. Sci. Eng. B* 131 (2006) 186–190.
- [28] J. Yang, B.F. Wang, K. Wang, Y. Liu, J.Y. Xie, Z.S. Wen, *Electrochim. Solid-State Lett.* 6 (2003) A154–A156.
- [29] P. Gu, R. Cai, Y.K. Zhou, Z.P. Shao, *Electrochim. Acta* 55 (2010) 3876–3883.
- [30] Y.X. Wang, S.L. Chou, J.H. Kim, H.K. Liu, S.X. Dou, *Electrochim. Acta* 93 (2013) 213–221.
- [31] B. Zhao, R. Cai, S.M. Jiang, Y.J. Sha, Z.P. Shao, *Electrochim. Acta* 85 (2012) 636–643.
- [32] M. Swietoslawski, M. Molenda, K. Furczon, R. Dziembaj, *J. Power Sources* 244 (2013) 510–514.
- [33] R. Mukherjee, R. Krishnan, T.M. Lu, N. Koratkar, *Nano Energy* 1 (2012) 518–533.
- [34] B. Fuchsbichler, C. Stangl, H. Kren, F. Uhlig, S. Koller, *J. Power Sources* 196 (2011) 2889–2892.
- [35] J. Lai, H.J. Guo, Z.X. Wang, X.H. Li, X.P. Zhang, F.X. Wu, P. Yue, *J. Alloys Compd.* 530 (2012) 30–35.